Molecular Catalysis 558 (2024) 114035

Contents lists available at ScienceDirect

Molecular Catalysis

journal homepage: www.journals.elsevier.com/molecular-catalysis

Research Paper

Modulating selectivity in CO2 Methanation through Rhodium catalysts supported on Zirconia-Chemically grafted SBA-15

K.A. Gómez-Flores [a,b], A. Solís-García [b], S.A. Jimenez Lam [a], M.E. Cervantes-Gaxiola [a], R. I. Castillo-López [a], J.P. Ruelas Leyva [a], S.A. Gómez [c], E. Flores-Aquino [b], T.A. Zepeda [b,*]

[a] Facultad de Ciencias Químico Biológicas, Universidad Autónoma de Sinaloa, Josefa Ortiz de Domínguez, Ciudad Universitaria, Culiacán, Sinaloa, 80013, México
[b] Centro de Nanociencias y Nanotecnología, Universidad Nacional Autónoma de México, Carretera Tijuana- Ensenada km 107, Ensenada B.C. 22800, México
[c] Departamento de Ingeniería de Procesos e Hidráulica, UAM–Iztapalapa, Av. San Rafael Atlixco No. 186, Col. Vicentina, Ciudad de México, 09340 México

ARTICLE INFO

Keywords:
CO_2 utilization
CO_2 methanation
CO_2 selectivity
Rh-based catalyst
In-situ FTIR
SBA-15

ABSTRACT

This study presents the impact of ZrO_2 incorporation on Rh-supported SBA-15 catalysts for CO_2 hydrogenation. ZrO_2 was chemically grafted onto the SBA-15 surface, varying concentrations of ZrO_2 from 5 to 20 wt.%. The ZrO_2-free catalyst favored CO production, leaning towards the reverse water gas shift reaction. The addition of ZrO_2 notably enhanced catalytic activity and led to a significant shift in selectivity towards methane production. The selectivity modulation is linked with the modified surface of SBA-15, covered with a ZrO_2 phase. The FTIR characterization under reaction conditions evidenced Rh-carbonyls formation in all samples. However, in catalysts materials with ZrO_2, formate species are also formed, probably promoted by the Zr-OH groups. A linear relation between formate species and the CH_4 selectivity suggests that the methane formation could be associated with the hydrogenation of formate species, while the desorption of carbonyls on Rh can explain the CO generation.

1. Introduction

It is clear that continued dependence on fossil fuels results in significant atmospheric CO_2 emissions and hastens climate change [1,2]. The challenges of rising CO_2 levels demand solutions that lead to reduced emissions, capture and convert CO_2 into value-added resources, offering a comprehensive approach to curbing persistent global warming [3–5]. Among these solutions, the strategy of harnessing atmospheric pollutants to produce renewable and clean energy is particularly notable [6–8]. Since CO_2 is a primary contributor to environmental pollution, numerous strategies have been proposed for its catalytic conversion into methane, methanol, higher alcohols, and hydrocarbons [8,9]. However, due to the inherent thermodynamic stability of the CO_2 molecule, its conversion becomes challenging and requires chemical reactions at elevated temperatures and pressures [10–12].

In 1902, Sabatier and Senderens [13] first documented that CO_2 methanation can occur at atmospheric pressure and temperatures below 400°C in the presence of a Ni catalyst. The CO_2 methanation seems like a simple reaction; however, parallel side reactions concurrently occur. Subsequently, Choi et al. [14] provided a comprehensive analysis of the catalytic CO_2 methanation process as described in Eq. (1):

$$CO_2 + 4H_2 \leftrightarrow CH_4 + 2H_2O \quad (1)$$

Simultaneously to the direct CO_2 methanation, the reverse water gas shift (RWGS) and CO methanation reactions can occur in parallel, represented by Eq. (2) and Eq. (3), respectively.

$$CO_2 + H_2 \leftrightarrow CO + H_2O \quad (2)$$

$$CO + 3H_2 \leftrightarrow CH_4 + H_2O \quad (3)$$

The principal challenge lies in designing catalysts that catalyze CO_2 methanation at lower temperatures and high conversion rates, while suppressing parallel reactions such as RWGS and CO hydrogenation. Aiming for this goal, several authors have thoroughly investigated the methanation of CO_2 catalyzed by various metals, such as Ru [15–19], Rh [20–22], Pd [23–25], and Ni [26–30], which are typically dispersed on the surfaces of metal oxides like ZrO_2 [23,26,31-32], TiO_2 [18,20,21, 30], CeO_2 [17,33-35], zeolites [22,36-37], Al_2O_3 [38], SiO_4 [39] and metal-organic frameworks [40–41]. These supports have demonstrated an impact on the catalyst activity, suggesting that they are frequently

* Corresponding authors.
E-mail address: trino@ens.cnyn.unam.mx (T.A. Zepeda).

https://doi.org/10.1016/j.mcat.2024.114035
Received 15 December 2023; Received in revised form 29 February 2024; Accepted 9 March 2024
Available online 20 March 2024

not inert and lead to complex metal-support interactions [42–43] and could even play an important role in the reaction mechanism during the CO_2 methanation [44–45].

Among the mentioned catalysts, zirconia-supported Rh catalysts are the most commonly used for CO_2 methanation due to their high activity and selectivity towards methane, suppressing the RWGS reaction and, consequently, the CO methanation pathway [46]. However, pure zirconia-based supports for preparing CO_2 methanation catalysts present one important disadvantage: these generally have a low surface area (typically ~20-125 m^2g^{-1}). In this sense, some studies reported the synthesis of amorphous zirconia supports with a significant specific surface area (190–240 m^2g^{-1}). However, these materials usually have low crystallinity and stability, which are not optimal to synthesize catalysts for the methanation of CO_2 [47–48].

Additionally, two strategies have been proposed for introducing zirconia into mesoporous material: (*i*) post-synthesis deposition using the incipient wetness impregnation of the zirconia precursor onto the surface [49–50] and (*ii*) in-situ modification with zirconia ions incorporation during the synthesis. However, these present drawbacks considerably limit their practical applications [51]. The former often results in particles with limited dispersion and weak surface interaction, while the latter weakens the structure stability when zirconia content exceeds 10 wt.%.

An alternative approach involves chemical grafting of ZrO_2 onto high-surface supports by the post-synthesis method, where heteroatom species are introduced to the surface of mesoporous materials. Several reports indicate that zirconia incorporation into the SBA-15 matrix through chemical grafting enables the deposition of highly dispersed ZrO_2 species onto the SBA-15 surface (450-700 m^2g^{-1}), modifying its chemical properties without significant changes to its structure and texture [52–54]. This ensures that it remains accessible for interactions with supported metal catalysts.

Therefore, the present work explores the impact of incorporating variable amounts of zirconium oxide (5-20 wt.%) onto the surface of SBA-15 using a post-synthesis chemical grafting method with the aim to synthesize Zr-modified samples with high dispersion on the SBA-15 molecular sieve surface, resulting in enhanced Rh dispersion and, thus, an increased CO_2 methanation activity. Furthermore, we hypothesize that the presence of zirconium oxide leads to the appearance of diverse surface species under reaction conditions, which can modify the reaction pathways toward different products.

2. Experimental

2.1. Synthesis of SBA-15 and chemical grafting of Zirconium-modified SBA-15 supports

SBA-15 was synthesized via sol-gel technique by dissolving 1.92 g of block copolymer (Pluronic 123) in 75 mL of a 4 M HCl solution at 35°C. Subsequently, 4 g of tetraethyl orthosilicate (TEOS) was incorporated into the mixture under robust stirring conditions and stirred for 24 h. The resulting sol was then exposed to hydrothermal treatment at 90°C for 24 h to produce the gel. After this, the product was filtered, dried at 110°C for 18 hours, and calcinated at 500°C for 6 h, with a heating rate of 1°C/min.

Zirconium (IV) propoxide (a 70 wt.% solution in 1-propanol) was used as the zirconia source. For the grafting process, calcined SBA-15 was mixed into this 1-propanol solution (with a ratio of 100 mL/g) and allowed to slurry for 8 h at room temperature. The material was subjected to three ethanol washes post-filtration to remove excess zirconium precursor. Finally, the solid was air-dried at room temperature and calcined in a static air environment at 550°C for 5 h. The samples were synthesized varying the ZrO_2 loadings of 5, 10, 15, and 20 wt.%.

2.2. Synthesis of Zirconium-modified SBA-15 supported Rh catalysts

The catalysts were synthesized through the wet impregnation method, using an $RhCl_3$ solution in deionized water with the appropriate concentration to achieve a 1 wt.% of Rh loaded. The support material was immersed in the $RhCl_3$ solution and stirred continuously at room temperature for one hour. Subsequently, the solvent was removed by heating at 80°C, and then the samples were dried at 100°C and calcined at 450°C for 5 h.

2.3. Characterization methods

The zirconia and rhodium content were quantified using an ICP-AES Perkin Elmer Optima 3300DV instrument.

Textural properties were evaluated using the N_2 adsorption-desorption isotherms at -196°C on a Micromeritics TRISTAR III system. Before the analysis, samples were pre-treated by outgassing at 200°C for 10 h.

X-ray diffraction measurements were performed using a PANalytical Aeris diffractometer outfitted with a Pixel 1D detector and a Cu Kα radiation source (λ = 1.5405 Å), with a step size of 0.021°/min, in the 2θ range of 10 to 80°.

The UV-vis diffuse reflectance spectroscopy (DRS UV-vis) measurements were carried out with an Agilent Cary-5000 UV-Vis spectrophotometer equipped with a Praying Mantis diffuse reflection reaction cell (Harrick Scientific).

Temperature-programmed reduction (TPR) analyses were conducted using a Quantachrome ChemBET Pulsar equipment. About 30 mg of the sample was first degassed at 150°C under a N_2 flow for 1 h. After cooling to room temperature, the TPR analysis was performed by heating the sample in a U-tube reactor to 650°C at 10°C/min in a 10% H_2/Ar mixture at 25 mL/min.

X-ray photoelectron spectra (XPS) were acquired using a SPECS® spectrometer with a PHOIBOS® 150 WAL hemispherical energy analyzer with sub-degree angular resolution (< 0.5°), equipped with both XR 50 Al-X-ray and μ-FOCUS 500 X-ray monochromator sources for Al excitation lines. Charge-related effects were adjusted by setting the C 1s peak binding energies of adventitious carbon to 284.5 eV.

TEM images of the samples were obtained using a JEOL JEM-2100F (STEM) microscope with energy dispersive X-ray spectroscopy (EDX), operating at 200 kV and 54 μA. The samples were pretreated in a 30 mL/min H_2 flow at 300°C for an hour. Then, they were dispersed in isopropanol using an ultrasonic bath. The resulting suspension was deposited onto a copper grid, and the solvent was evaporated at room temperature.

2.4. Catalytic evaluation

Catalytic evaluations were measured in a specially designed packed bed reactor, linked in real-time to a Shimadzu 12-A chromatograph with a thermal conductivity detector (TCD), using 5A and Porapack Q packed columns. 60 mg of catalyst was placed in a microreactor with an internal diameter of 6 mm. The catalyst was treated in situ at 300°C for 1 h under 30 mL/min of H_2 flow. Following the reduction stage, the catalyst was cooled to an initial reaction temperature of 150°C. The gas flow was then switched to a reactive mixture of 20% CO_2 and 80% H_2, achieving a 1:4 molar ratio of CO_2:H_2 with a flow rate of 15 mL/min. The gas hourly space velocity (GHSV) was set at 15,000 h^{-1} for these experiments. The catalytic activity was evaluated by means of CO_2 conversion (X_{CO_2}) and selectivity towards CH_4/CO products (S_{CH4} or S_{CO}) under steady-state conditions from 150°C to 300°C. These parameters were calculated according to the following Eqs. (4-6):

$$X_{CO_2}(\%) = \frac{F_{CO_2}in - F_{CO_2}out}{F_{CO_2}in} x100 \quad (4)$$

$$S_{CH_4}(\%) = \frac{F_{CH_4}out}{F_{CO_2}in - F_{CO_2}out} x100 \quad (5)$$

$$S_{CO}(\%) = \frac{F_{CO}out}{F_{CO_2}in - F_{CO_2}out} x100 \quad (6)$$

Where F_i represents the molar flow rate of each component, either at the inlet or the outlet, measured in mol/s. As outlined in our prior report, the Axial Dispersion Criterion (ADC) was calculated using the Mears equation to evaluate possible mass transfer limitations [46].

2.5. FTIR characterization under reaction conditions

The FTIR spectroscopy characterization under reaction conditions was performed in an Agilent 660 spectrophotometer equipped with a transmission cell/flow reactor ISRI and CaF_2 windows. Self-supporting wafers of the catalysts with a thickness of 40 mg cm^{-2} were prepared by pressing the powdered samples at a pressure of 10 tons. Before CO_2 methanation experiments, the self-supporting wafers were treated with 40 mL/min of a reducing mixture (20% H_2, balance N_2) at 300°C for 1 h. Then, the samples were cooled down to 150°C. For the CO_2 methanation experiments, the reduced samples were exposed to 40 mL/min of the reaction mixture (6.25% CO_2/ 25% H_2/ 68.75% N_2 vol/vol) while the temperature of the FTIR cell/flow reactor was increased from 150 to 300°C, at a heating rate of 2°C/min. The IR spectra were recorded with a resolution of ±4 cm^{-1}.

3. Results and discussions

3.1. Characterization of the samples

Table 1 presents the labeling, textural properties, and chemical composition of the synthesized supports and catalysts. Theoretical ZrO_2 loadings for the synthesized materials were set at 5, 10, 15, and 20 wt.%. The actual ZrO_2 contents in the synthesized materials closely matched the theoretical content up to a 15 wt.% ZrO_2 loading, meaning the effective ZrO_2 incorporation onto the SBA-15 surface up to this load. For ZrO_2 loadings exceeding 15 wt.%, complete grafting of Zr species onto the SBA-15 material was not achievable, probably due to surface saturation. This saturation appeared to occur around 18.8 wt.% ZrO_2 loading. It is important to mention that any excess alkoxides lacking chemical interaction with OH groups were removed through washing with dry ethanol. The grafting method for Zr onto SBA-15 involves a chemical bonding between cationic Zr species and the silanol (Si-OH) groups present on the SBA-15 surface. This process leading to the formation of Zr-O-Si- surface species through a condensation reaction. Subsequently, ignoring the concentration of Zr species, the condensation process continues, giving rise to the surface formation of Zr-O-Zr species, gradually covering the surface of the SBA-15. In subsequent stages, a calcination stage is carried out in a static oxidation environment to eliminate organic residues and finish oxidizing the cationic Zr species towards the formation of highly dispersible ZrO_2 species on the surface. Such chemical interactions not only secure ZrO_2 onto the surface but also potentially influence the chemical environment of the SBA-15, affecting its catalytic properties.

Table 1
Labeling, composition[a] and textural properties of the samples.

Material	Labeling	Composition		S_{BET} (m^2 g^{-1})	V_p (cm^3 g^{-1})	d_p (nm)
		ZrO_2 (wt.%)	Rh (wt. %)			
SBA-15	S	-	-	845	1.06	7.2
SBA-15; Zr 5 wt.%	SZr05	4.6	-	814	0.99	7.0
SBA-15; Zr 10 wt.%	SZr10	9.5	-	738	0.96	6.7
SBA-15; Zr 15 wt.%	SZr15	14.7	-	685	0.89	6.5
SBA-15; Zr 20 wt.%	SZr20	18.8	-	628	0.81	6.2
Rh/SBA-15	C	-	0.97	845	1.04	7.1
Rh/SBA-15; Zr 5 wt.%	CZr05	4.5	0.98	817	1.00	6.9
Rh/SBA-15; Zr 10 wt.%	CZr10	9.4	0.96	728	0.97	6.6
Rh/SBA-15; Zr 15 wt.%	CZr15	14.6	0.95	689	0.86	6.3
Rh/SBA-15: Zr 20 wt.%	CZr20	18.6	0.94	624	0.82	6.0

[a] Obtained from ICP-AES

The N_2 adsorption-desorption isotherms for both supports and catalysts, depicted in Fig. S1 of the supplementary information (SI), exhibit type IV profiles with H1 hysteresis loops according to the IUPAC classification [52]. Such isotherm patterns indicate the well-structured nature of the SBA-15 materials. The bare SBA-15 sample (S sample) exhibited the higher surface area (S_{BET}), 845 m^2/g (Table 1). The grafting of ZrO_2 onto the SBA-15 surface reduces the S_{BET} value, exhibiting a gradual decrease related with the rising ZrO_2 content. The most significant decreases in surface area, dropping up to 217 m^2/g, occurred in the sample with the highest ZrO_2 content (SZr20). Grafting ZrO_2 onto the SBA-15 surface also reduces the average pore diameter (d_p) as a function of ZrO_2 content (Table 1). As the ZrO_2 content increases, the pore size distribution becomes narrower (Fig. 1a), this indicates the potential blockage of smaller pores by ZrO_2 particle deposition. As expected, the pore volume (Vp) values also show a gradual decrease with increasing ZrO_2 loaded. After the rhodium was deposited, no significant changes in the values of the textural properties were observed (Table 1), and even the narrow distribution of dp values was preserved (Fig. 1b).

The small-angle X-ray diffraction pattern of the synthesized SBA-15 material displays three distinct peaks typical for SBA-15-type materials (Fig. 2a). These include a pronounced peak at approximately 0.95° (2θ) and two weaker peaks observed between 1.6° and 1.9° (2θ). The diffraction peaks are identified as the (100), (110), and (200) reflections, respectively, indicative of p6mm hexagonal symmetry. The intense (100) peak corresponds to a d-spacing of 9.6 nm (close to that observed by the N_2 isotherms), while the (110) and (200) peaks yield d-spacing of 5 nm and 4.4 nm, respectively [55]. These measurements are in line with a two-dimensional hexagonal pore arrangement [56].

Consistent with these findings, the HRTEM images in Fig. 3 reveal that the materials possess a well-ordered hexagonal arrangement of mesopores, forming a cylindrical pore structure. For supports with higher ZrO_2 content (SZr15 and SZr20 samples), a slight shift to higher angles and a reduction in peak intensity were noted, particularly pronounced in the SZr20 sample. This shift suggests a lower expansion in the lattice structure and a decrease in pore diameter, likely due to the ZrO_2 graft coating the SBA-15 surface, as detailed in Table 1. However, it is important to know the location of zirconium oxide species within SBA-15 is crucial, dark-field TEM imaging was employed for the SZr10 and SZr20 samples, as shown in Fig. S2. These images offer insights into the dispersion and locations of ZrO_2, predominantly within the SBA-15 structure. Nonetheless, the possibility of ZrO_2 species also forming on the external surface of the material has not been discarded.

Similar small-angle X-ray diffraction patterns for the catalysts were observed (Fig. S3a). This implies that the incorporation of small amounts of rhodium does not substantially modify the structure of the corresponding support. The powder wide angle X-ray diffraction patterns for the ZrO_2-modified supports and catalysts are shown in Fig. 2b and supplementary Fig. S3b, respectively. Regardless of the ZrO_2 content, a broad line was observed between 15° and 35° (2θ), characteristic of the amorphous siliceous phase [57]. For both the ZrO_2-modified supports and catalysts, no reflections characteristics of zirconia oxide or rhodium phases were detected, indicating the effective dispersion of

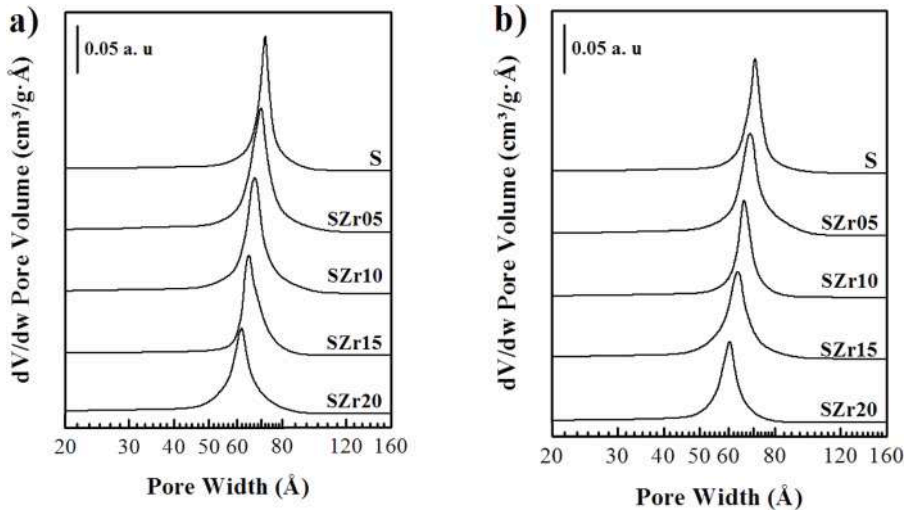

Fig. 1. Pore size distribution derived from the desorption branch of the bare supports a) and Rh-supported catalysts b).

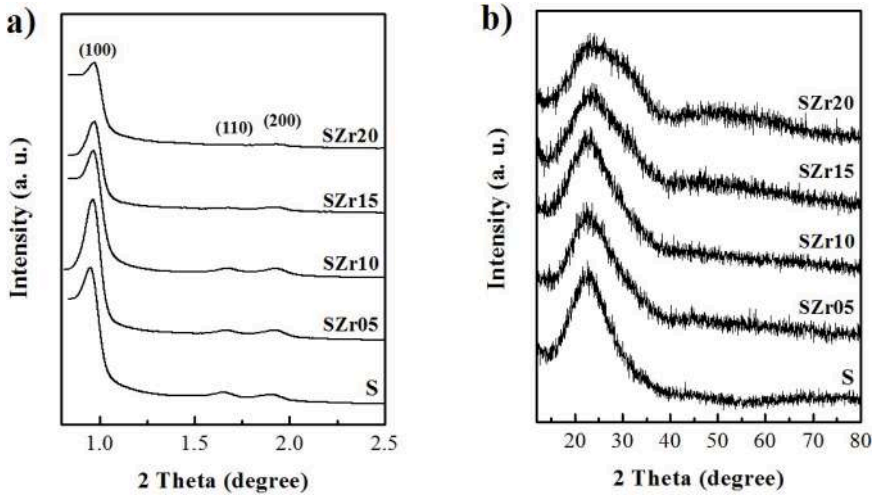

Fig. 2. Low-Angle a) and Wide-Angle b) XRD Patterns for the bare supports.

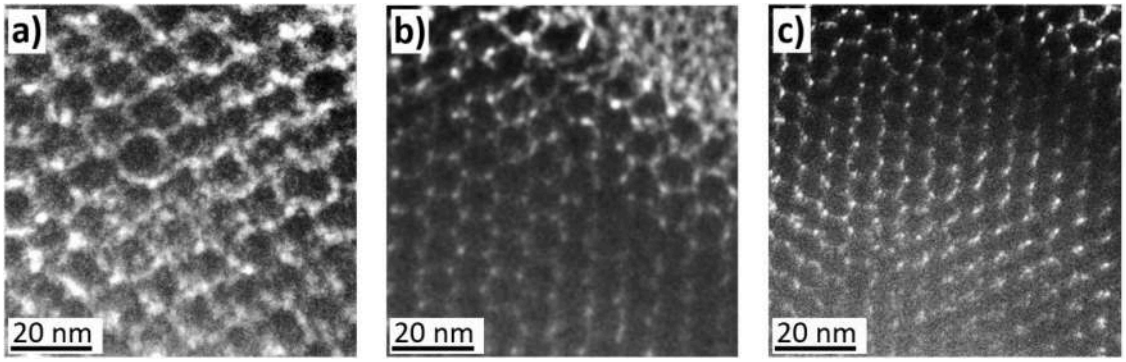

Fig. 3. Representative High-Resolution TEM Images for the S a), SZr10 b), and SZr20 c) supports.

these species on the surface.

The UV-vis DRS analysis of the ZrO_2-grafting catalysts suggests well-dispersed zirconium ions, as indicated by the spectra shown in Fig. S4. For catalysts with lower ZrO_2 grafting (specifically the CZr05 sample), an absorption peak at 202 nm was observed. This peak is associated with the charge transfer transition from O^{2-} to Zr^{4+} in highly dispersed Zr^{4+} ions located in isolated tetrahedral environments [52]. As the ZrO_2 load increased, the absorption peak corresponding to the O^{2-} to Zr^{4+} charge transfer transition shifted towards a higher wavelength. Particularly in the CZr20 sample, this peak appeared around 207 nm. Such a red-shift in absorption indicates a reduced dispersion of zirconium species and an increased coordination number, likely due to the formation of Zr–O–Zr species, indicating the formation of larger zirconium oxide structures [58].

X-ray photoelectron spectroscopy (XPS) on freshly reduced samples was conducted to identify the surface zirconium oxide species present as a function of ZrO_2 loaded. XPS spectra of the Zr 3d core electron levels of freshly reduced catalysts are presented in supplementary Fig. S5a. Binding energy (BE) values for Zr 3d and Rh 3d core electrons and the surface atomic ratios of Zr/Si and Rh/Si for the freshly reduced catalysts are presented in Table 2. In all catalysts, the Zr $3d_{5/2}$ peak displays a component at approximately 182.4 ± 0.1 eV, close to bulk ZrO_2 [58–60]. Nevertheless, an additional peak around 183.5 eV was observed in samples with lower ZrO_2 content (CZr05 and CZr10 samples). The presence of a signal at a higher BE value (183.5 eV), compared to the typical BE of the ZrO_2 bulk phase (182.4 eV), suggests an alteration in the electronic environment of the zirconium species. This shift could be attributed to the formation of Si – O – Zr species [58–60]. Since that the Si atom has higher electronegativity than the Zr atom, there is a greater localization of electron clouds around the Si atoms. This electron cloud localization towards the Si atoms results in an increase in the BE value.

The signal associated with Si-O-Zr species represents approximately 38% in the sample with the lowest ZrO_2 content (CZr05 sample). Notably, this signal diminishes significantly as the ZrO_2 content increases, potentially due to the surface becoming increasingly coated with the ZrO_2 phase. Given that XPS is a surface-sensitive technique; its ability to detect such changes is inherently constrained, especially under conditions of substantial surface coverage, as suggested by the Zr/Si atomic dispersion results (Table 2). These results suggest that a fraction of zirconium species grafted onto the SBA-15 structure may bond to surface Si atoms, with some zirconium atoms potentially integrating into the framework of SiO_2 initial atomic layers. Such interactions result in the formation of surface Si-O-Zr linkages and Zr-OH groups. Additionally, the formation of surface Zr-O-Zr species linkages becomes increasingly evident with higher ZrO_2 loadings.

Fig. 4 shows the H_2-TPR profiles of the calcined catalysts. It is observed that all the catalysts exhibit intense reduction peaks of H_2 consumption, ranging between 147-168°C, which can be attributed to the reduction of the Rh_2O_3 phase into Rh^0 species [61–62], which was confirmed by XPS. The Rh 3d core electrons, as shown in Fig. S5b, exhibit a pronounced peak at approximately 307.2 ± 0.1 eV (Table 2), indicative of metallic rhodium species [63–64]. The highest reduction temperature for this peak was noted in the rhodium-free sample at 168°C. As the ZrO_2 load increased, a gradual decrease in the reduction temperature of this signal was observed, dropping to 146°C for the sample with the highest ZrO_2 content (CZr20). This observation implies that the incorporation of ZrO_2 lightly decreases the interaction between rhodium oxide species and the surface. Additionally, the amount of H_2 consumed during this reduction process increased proportionally with the ZrO_2 content. Additionally, the amount of H_2 uptake during this reduction process increased as a function of the ZrO_2. The trend in H_2 uptake between 147-168°C was as follows: C (21.5 mmol/g) < CZr10 (21.9 mmol/g) < CZr15 (22.6 mmol/g) < CZr20 (23.1 mmol/g). This trend could indicate that the presence of ZrO_2 enhances the dispersion of rhodium species. This finding is consistent with the Rh/Si surface atomic dispersion data obtained from XPS (detailed in Table 2). In this sense, it can be inferred that the addition of ZrO_2 modulates the interaction between oxide rhodium species and the surface, leading to a considerable enhancement in the dispersion of rhodium species across the surface.

Table 2
Binding energies (eV) of Zr 3d and Rh 3d core electrons and the surface atomic ratios of Zr/Si and Rh/Si for the freshly reduced catalysts.

Sample	Zr $3d_{5/2}$	Rh $3d_{5/2}$	Zr/Si atomic	Rh/Si 10^{-3} atomic
C	-	307.3	-	7.3
CZr05	182.5 (62%) 183.5 (38%)	307.2	0.032	7.6
CZr10	182.4 (82%) 183.5 (18%)	307.1	0.054	7.9
CZr15	182.3 (100%)	307.2	0.076	8.3
CZr20	182.2 (100%)	307.3	0.098	8.5

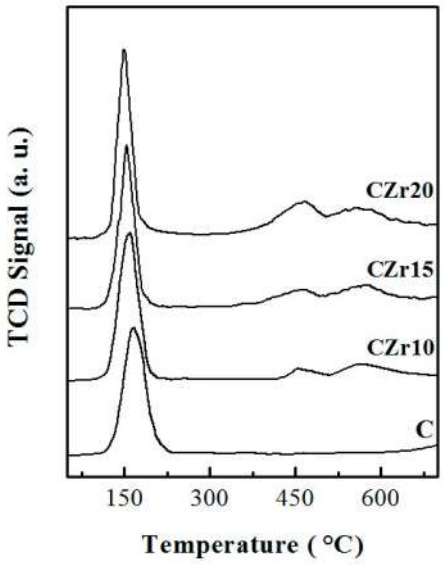

Fig. 4. TPR profiles for the Rh-supported Catalysts.

TEM-EDX analysis was performed on the freshly reduced highest ZrO_2 content sample (CZr20) to evaluate the surface distribution of zirconium and rhodium species. The representative STEM and elemental mapping images are shown in Fig. 5. Fig. 5a shows a representative section for analysis, while Figs. 5b and 5c display the elemental mapping of rhodium and zirconium species, respectively. A quantitative breakdown of these species is provided in Fig. 5d. The elemental maps (Figs. 5b and 5c) indicate a uniform distribution of rhodium and zirconium species on the surface.

The atomic analysis in Fig. 5d reveals a composition of 0.37% Rh, 5.82% Zr, 43.39% Si, and 50.42% O, translating to an approximate weight composition of 1.1% metallic Rh (assuming complete reduction, as supported by XPS data), 21.3% ZrO_2, and 77.6% SiO_2. These results are in line with the bulk composition determined by ICP-AES (Table 1), confirming the uniformity of the catalyst's surface composition.

Additionally, in the samples containing ZrO_2, two additional reduction peaks were observed at 453°C and 573°C. The intensity of the TCD signal for these peaks intensified in proportion to the increase in ZrO_2 content. These reduction peaks, characterized by their poor hydrogen uptake, are typically indicative of both surface and bulk reduction of the lattice oxygen in zirconia [65–66]. As expected, hydrogen consumption escalates with the rise in ZrO_2 content. However, this oxygen desorption stage occurs at temperatures exceeding those employed for the CO_2 hydrogenation reaction (300°C). It is believed that such high-temperature desorption is unlikely to interfere with the reaction mechanism.

3.2. *CO_2 methanation catalyzed by Zr-chemically grafted SBA-15 supported Rh*

The supported Rh samples were tested as catalysts for the CO_2 hydrogenation reaction in a continuous flow-packed bed reactor. Fig. 6 shows the CO_2 conversion as a function of temperature. To further illustrate the impact of Zr-chemically grafted SBA-15 supported Rh on catalytic performance, we have included the activity of the Rh/ZrO_2 and Rh/SiO_2 catalysts, each prepared with a 1% Rh loading by weight. In the 175 to 300°C range, under the conditions employed in this study, all materials demonstrated activity in the catalyzed CO_2 hydrogenation, generating CH_4 and CO as the products. As expected, an increase in the

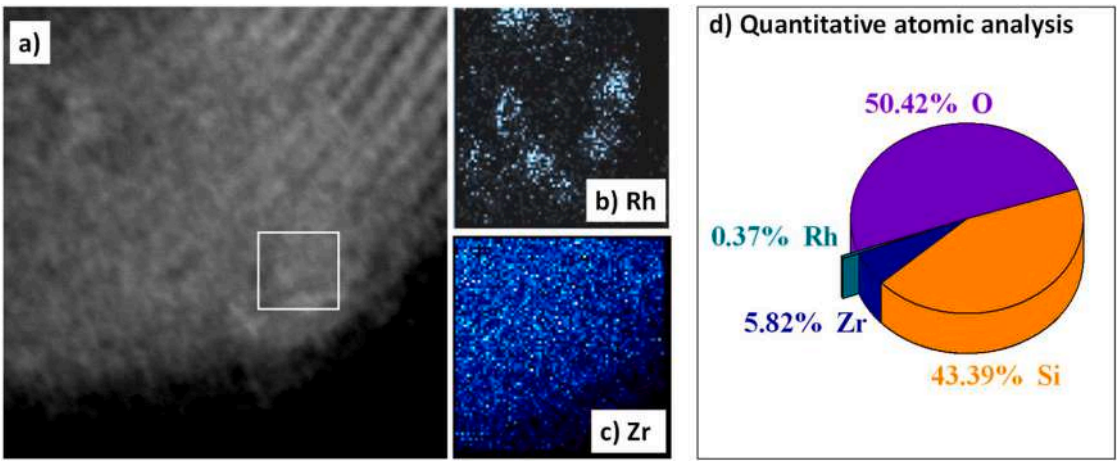

Fig. 5. a) Representative STEM image for the CZr20 catalysts; b-c) STEM-EDX elemental mapping images of Rh and Zr; d) distribution of quantitative analysis

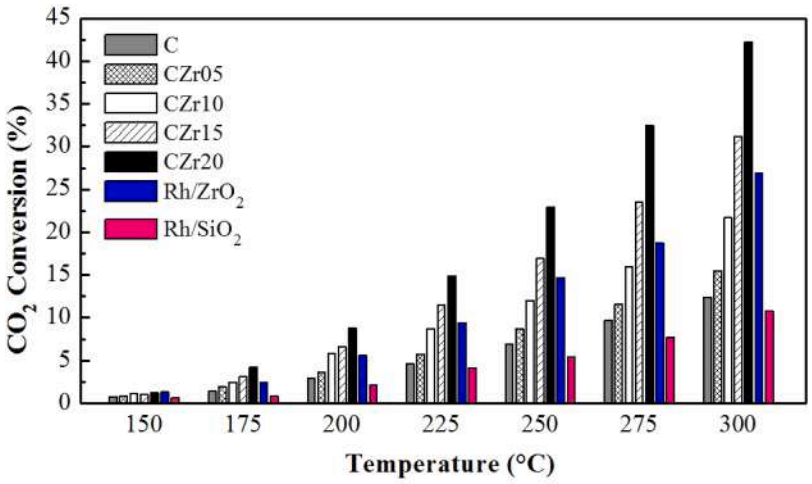

Fig. 6. Steady-state CO_2 conversion over Rh-supported catalysts. GHSV= 15,000 h^{-1}, H_2:CO_2=4:1.

reaction temperature corresponded to a rise in the percentage of CO_2 conversion, as depicted in Fig. 6. The rhodium catalyst supported on zirconium-free SBA-15 demonstrated superior performance compared to those prepared on amorphous silicon oxide, indicating the significance of the support material in enhancing catalytic efficiency.

Notably, the CO_2 conversion increased gradually with the incorporation of ZrO_2 on the surface of SBA-15, as observed in Fig. 6. Upon comparing the catalytic activity of Rh supported on Zr-chemically grafted SBA-15 against a standard Rh/ZrO2 catalyst, it was observed that the CZr15 and CZr20 catalysts demonstrated significantly enhanced performance, particularly at higher temperatures. However, the profile of the obtained products was different in all samples. As detailed in

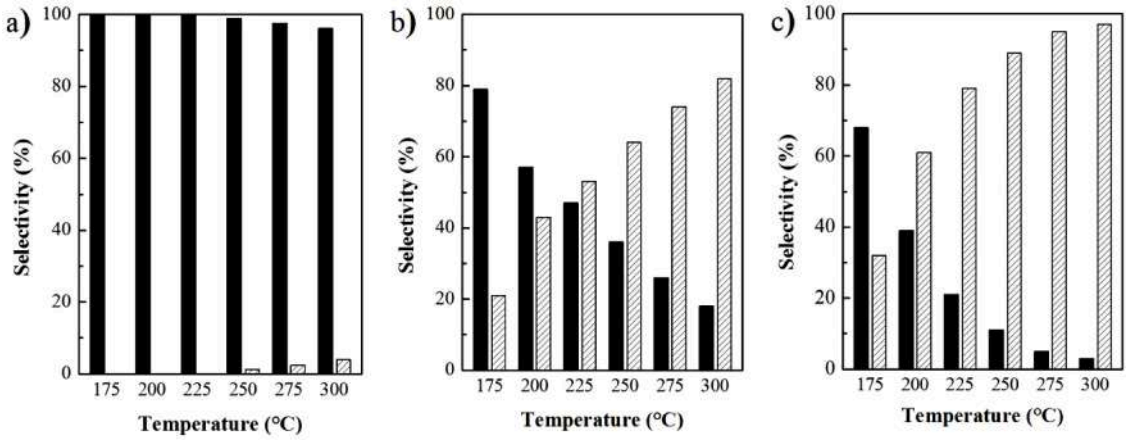

Fig. 7. Selectivity towards CH_4 and CO of the representative samples (CO; CH_4). a) C; b) CZr10; CZr20.

Fig. 7a, carbon monoxide was the main product in the Rh/SBA-15 since a small amount of methane was produced only above 250°C. In contrast, the Rh/SiO_2 catalyst demonstrated total selectivity towards CO production across all tested temperatures.

On the other hand, the reference catalyst Rh/ZrO_2 showed complete selectivity towards methane production across all tested temperatures, while Rh supported on Zr-chemically grafted SBA-15 displayed an increased selectivity for methane (CH_4) as the ZrO_2 loading was raised (Figs. 7b and 7c). This observation suggests an interplay between the surface composition and its selectivity profile, with ZrO_2 loading directly influencing methane production efficiency and inhibits the reverse water gas shift reaction. It is important to highlight that in all cases, the selectivity to methane increased simultaneously with the temperature increment (Fig. 7). In contrast, an opposite behavior was observed in the CO selectivity, decreasing with the temperature increase (Fig. 7). Therefore, at the conditions used in this study, the CO production occurs at low temperatures, while that higher temperature enhances the formation of CH_4. Possibly, the CO produced by the catalysts is completely hydrogenated at higher temperatures.

3.4. FTIR characterization during CO_2 hydrogenation

To obtain more details about how the addition of zirconium oxide to Rh supported on SBA-15 samples modifies the selectivity, the surface species formed under reaction conditions were determined by in situ FTIR characterization.

3.4.1. Analysis of Zr-free catalyst

Fig. 8 shows the FTIR characterization of the Rh supported on the SBA-15 sample. When the reactive mixture (6.25% CO_2/ 25% H_2/ 68.75% N_2 vol/vol) entered the FTIR reactor/cell at 175°C, several bands emerged in the IR spectra as detailed in Fig. 8. The presence of CO_2 in the cell was evidenced by the intense band at 2363 cm^{-1} attributed to the $\upsilon_{(CO2)}$ of the vibration mode of CO_2 in the gas phase [67]. On the other hand, the bands located at 2016 and 1814 cm^{-1} (Fig. 7c) have been assigned to the stretching of the C-O bond ($\upsilon_{(CO)}$) of carbonyl species bonded to Rh^0 in linear and bridged configuration, respectively [68,69]. The rise of these bands suggests that a portion of carbon dioxide is adsorbed dissociatively on the surface of metallic rhodium to produce COads (and O_{ads}).

Besides, two weak bands at 1608 and 1384 cm^{-1} were detected in the fingerprint region, as shown in Fig. 8c. These signals have been assigned to $\upsilon_{a(CO3)}$ and $\upsilon_{s(CO3)}$ vibration modes of carbonate species in bidentate configuration [67]. According to Fig. 8c, the intensity of the bands associated with Rh-carbonyls (2016 and 1814 cm^{-1}) is higher than those of carbonate species (1608 and 1384 cm^{-1}). This demonstrates that the CO_2 is preferentially adsorbed on the rhodium sites (dissociatively) than on the support (SBA-15).

As the temperature increases, the bands of Rh-carbonyl species (in linear and bridged form) gradually increased their intensity, reaching their maximum values at 250°C (Fig. 8c). Above this temperature, their intensities decreased slightly. Simultaneously, a new band at 3015 cm^{-1} with poor intensity emerged in the C-H stretching region, which has been assigned to the $\upsilon_{(CH)}$ of methane gas [70]. The decrease of the bands of carbonyl species on Rh^0 (2016 and 1814 cm^{-1}, Fig. 8c) matches the increment in the intensity of the band of CH_4 (3015 cm^{-1}, Fig. 8a). It is inferred that the Rh-carbonyl species can be involved in methane formation, possibly via a reaction between CO_{ads} with H adatoms, obtained by the H_2 dissociation on the surface of Rh sites. In the catalytic tests, CO gas was formed as the main product. However, no evidence of this compound was observed in the IR spectra. As observed in Fig. 8c, the bands associated with bidentate carbonate species (on SBA-15) increased during the experiment. This behavior is characteristic of surface spectator species, which do not participate in the catalysis. Unlike the catalytic tests, no evidence of CO gas was observed in the IR spectra (Fig. 8c). Instead, bands of methane emerged. This can be explained by the lower IR absorption coefficient of carbon monoxide than methane [71].

3.4.2. Analysis of CZr10 catalyst

The IR spectra obtained under reaction conditions of the CZr10 catalyst at increasing temperature are shown in Fig. 9. The contact between the mixture (6.25% CO_2/ 25% H_2/ 68.75% N_2 vol/vol) and the surface of the CZr10 at 175°C caused the appearance of similar bands to those observed in the Zr-free catalyst. Namely, CO_{2gas} (2363 cm^{-1}), Rh-carbonyls (2016 and 1814 cm^{-1} in linear and bridged configuration, respectively), and bidentate carbonate species (1610 cm^{-1}). As mentioned above, carbonyl and carbonate species can be formed due to the CO_2 adsorption on Rh sites and SBA-15, respectively. Also, an additional band at 1572 cm^{-1} was detected (Fig. 9c). Its assignment can be due to the $\upsilon_{a(CO2)}$ vibration mode of surface formate species on ZrO_2 [72,73]. The formation of these species (formate) can be explained by i) the reduction of bicarbonate species (by H atoms) or ii) the migration of CO_{ads} from Rh^0 to hydroxyl groups on ZrO_2 [74,75]. Notably, in Fig. 9a, it is possible to observe the band characteristic of methane gas (Fig. 9a), demonstrating that the incorporation of ZrO_2 to Rh supported on SBA-15 increases the catalytic activity, as was observed in the catalytic tests (Figs. 6 and 7).

Fig. 9 shows that the temperature increment in the FTIR cell promoted several changes in the IR spectra. The bands of carbonyl species (2016 and 1814 cm^{-1}, Fig. 9c) decreased gradually until 250°C. At higher temperatures, this decrease was more pronounced. The same

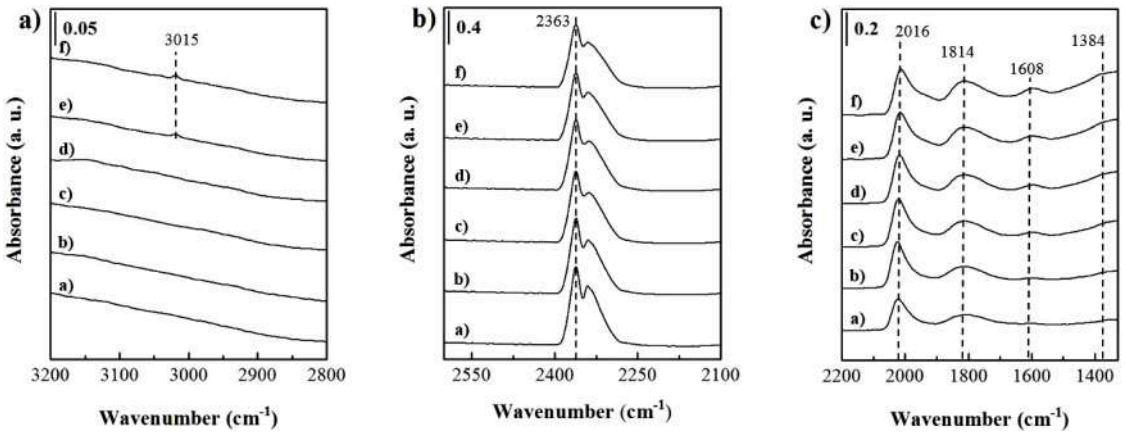

Fig. 8. FTIR characterization of the reduced Zr-free catalyst (C sample) under reaction conditions (gas mixture of 3% CO_2/ 12% H_2/ 85% N_2 vol/vol) at increasing temperature. a) 175°C; b) 200°C; c) 225°C; d) 250°C; e) 275°C; f) 300°C.

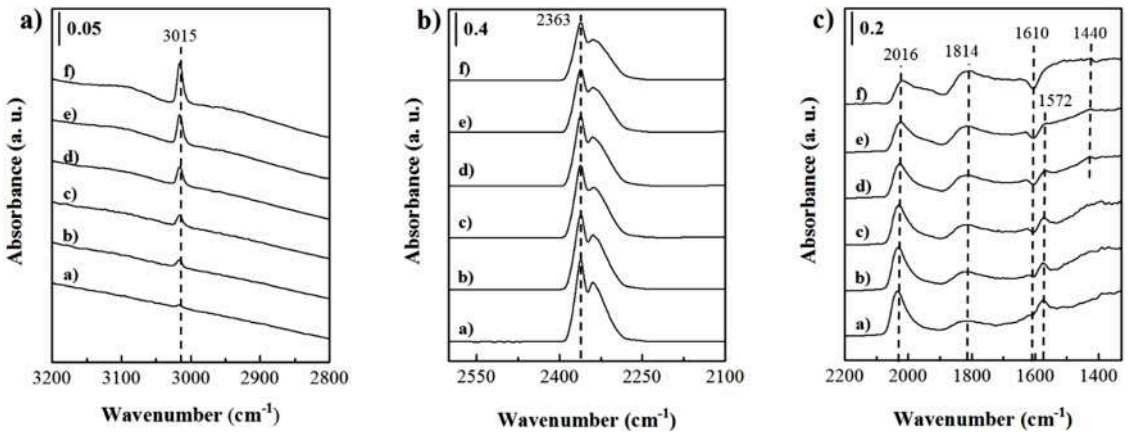

Fig. 9. FTIR characterization of the reduced CZr10 catalysts under reaction conditions (gas mixture of 3% CO_2/ 12% H_2/ 85% N_2 vol/vol) at increasing temperature. a) 175°C; b) 200°C; c) 225°C; d) 250°C; e) 275°C; f) 300°C.

trend was observed in the IR signals of formate species on ZrO_2 and CO_2 (1574 and 2363 cm^{-1}, Fig. 9c). Simultaneously, the intensity of the band of methane grew mainly above 250°C (3015 cm^{-1}, Fig. 9a). This behaviour suggests that both the Rh-carbonyls (linear and bridged) and the formate species (on ZrO_2) can be hydrogenated to CH_4 (by Hadtoms derived from H_2 adsorption on Rh sites).

Unlike the Zr-free catalyst, in this sample, the temperature increase promoted that the band of carbonate species in a bidentate form on SBA-15 (1610 cm-1, Fig. 9c) decreased until it disappeared. Possibly, these species can be transformed to surface formate in the vicinity of ZrO_2, given that in the Rh/SBA-15 sample, they did not decrease; thus, it is assumed that they cannot be transformed to carbonyl species on Rh. In addition, a new band at 1440 cm^{-1}, attributed to polydentate carbonate species on ZrO_2 [76], emerged and stayed constant along the experiment (Fig. 9c). Therefore, it is inferred that they act as spectators and they do not participate actively in the catalysis.

3.4.3. Analysis of CZr20 catalyst

The sample with the highest selectivity towards methane (CZr20) was also characterized by FTIR spectroscopy under reaction conditions. The obtained results are shown in Fig. 10. The interaction between the reactive mixture (6.25% CO_2/ 25% H_2/ 68.75% N_2 vol/vol) and the sample at 175°C led to the rise of bands of Rh-carbonyls in linear and bridge form (2016 and 1880 cm^{-1}, Fig. 10c), indicating that the CO_2 is adsorbed dissociatively on the metallic rhodium surface. The intensity of the band at 1572 cm^{-1} associated with the $\upsilon_{a(CO2)}$ vibration mode of surface formate species was highest compared to the other tested samples since the load of ZrO_2 was superior. The formate species on this sample was bolstered by an additional band at 1384 cm^{-1}, attributed to the $\upsilon_{s(CO2)}$ vibration mode [72,73]. As mentioned above, the formation of these species can be due to the reduction of bicarbonate species or by the reaction between carbonyls (on Rh) and hydroxyl groups on the support (ZrO_2) [74,75]. Fig. 10a shows that in this sample, methane is formed from 175°C, as was evidenced by the band at 3015 cm^{-1}, in accordance with the catalytic tests (Figs. 6 and 7). In addition, an intense band at 1612 cm^{-1} emerged, similar to those observed in the spectra of the Zr-free catalyst, which can be attributed to carbonate species ($\upsilon_{a(CO3)}$) bonded to the SBA-15 surface in bidentate form.

During the heating, the bands of Rh-carbonyls and formate species decreased sharply (Fig. 10c). Besides, the band of CO_2 gas 2363 cm^{-1} (Fig. 10b) diminished while the band of methane increased markedly, reaching the highest value among all examined samples (Figs. 8a, 9a, and 10a). Thus, it is inferred that both Rh-carbonyls and formate species can be involved in the transformation of CO_2 to CH_4. These observations suggest that, as described previously, the ZrO_2 promotes the hydrogenation of species derived from the CO_2 adsorption.

The intensity of the band associated with bidentate carbonate species on SBA-15 increased with the temperature increase (Fig. 10c). Hence, it is deduced that it does not participate in the catalysis. However, the intensity of this band was higher than in the other catalysts. Therefore, the incorporation of ZrO_2 improves CO_2 adsorption, generating also a kind of surface carbonate species that are not involved in this reaction. As observed in Fig. 10c, polydentate carbonate on ZrO_2 was formed at higher temperatures, as evidenced by the band at 1440 cm^{-1} [76].

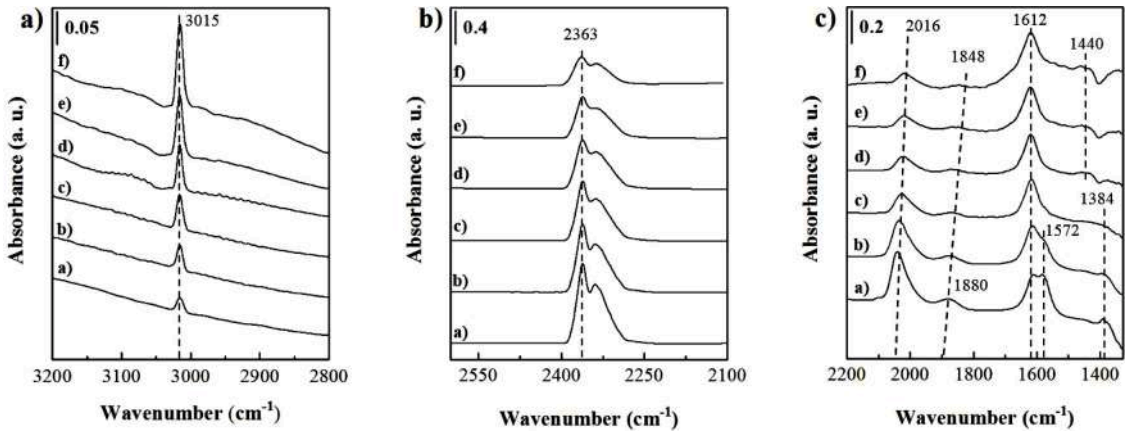

Fig. 10. FTIR characterization of the reduced CZr20 catalysts under reaction conditions (gas mixture of 3% CO_2/ 12% H_2/ 85% N_2 vol/vol) at increasing temperature. a) 175°C; b) 200°C; c) 225°C; d) 250°C; e) 275°C; f) 300°C.

Whose role in this reaction is as a spectator, since the intensity increased together with the temperature increase even when the methane was produced.

3.5. Plausible mechanism for CO_2 methanation on Rh-catalyst supported on Zirconia-chemically grafted SBA-15

The data in the last sections show that the grafting of ZrO_2 on the SBA-15 modifies the catalytic activity of the supported Rh samples. In specific, the selectivity varies notably with the addition of zirconium oxide. Without ZrO_2, the Rh/SBA-15 sample inclines the selectivity mainly towards carbon monoxide (Fig. 7a). With the incorporation of zirconium oxide, the selectivity to methane increases gradually (Figs. 7b and 7c). These observations suggest that in the pure catalyst (Rh/SBA-15), the CO_2 hydrogenation proceeds via RWGS reaction, generating carbon monoxide as a result, while on grafted samples, the ZrO_2 promotes the catalysis of the CO_2 methanation; in this case, methane is formed as a product. The FTIR characterization under reaction conditions showed that only Rh-carbonyl species act as intermediates in the sample of the rhodium supported in SBA-15 (in linear and bridge configuration, Fig. 8). For the case of the grafted catalysts, in addition to Rh-carbonyls, surface formate species were observed. According to our FTIR results, the formation of these species increases progressively with the increment of the ZrO_2 since the intensity of the $\upsilon_{a(CO2)}$ band of formate species grows linearly in the function of zirconium oxide load, as detailed in Fig. 11a.

In the CO_2 hydrogenation reactions catalyzed by supported metals, two proposals have been suggested regarding the origin of formate species: (*i*) the reduction of bicarbonate species generated by the reaction between CO_2 and surface hydroxyl groups and (*ii*) the result of the interaction of CO_{ads} (or CO_{gas}) with surface OH species. In both cases, the source of these species has been associated with the presence of hydroxyl groups on the support. Although these groups are on the surface of all samples tested in this study, in the form of Si-OH and Zr-OH, evidenced by the bands of 3728 and 3660 cm^{-1}, respectively (Fig. S6) [77,78]. It is evident that in the Rh/SBA-15 sample, the silanol groups cannot react with CO_2 or CO, given that bands associated with formate species were not detected in the IR spectra (Fig. 8c). In contrast, in the samples with ZrO_2, the generation of formate species increased in function of their load (Fig. 11a). This can be explained by an increment in the concentration of surface Zr-OH groups since the band at 3660 cm^{-1} is more resolved in the function of ZrO_2 load (Fig. S6).

As mentioned above, in the grafted samples, the selectivity towards methane increases simultaneously with the amount of surface ZrO_2. In this kind of samples, the bands of surface formate species formed due to their interaction with the reactive mixture were intensified with increasing zirconium oxide content. Thus, it is possible to determine a relation between the surface formate species (evidenced by the band at 1575 cm^{-1}) and selectivity to methane, which has a linear behavior (Fig. 11b). Therefore, it is possible to assume that the formate species are the main responsible for the methane formation in our samples (at the conditions used in this study) since in those materials where the formation of these surface species was null or poor carbon monoxide is produced preferentially, possibly due to that the carbonyls species are desorbed as CO_{gas}.

Based on the results obtained in this study, we have proposed a plausible reaction route for the CO_2 hydrogenation in the Rh-catalysts supported on Zr-chemically grafted SBA-15 (Fig. 12). The process begins with the adsorption of CO_2 and H_2 on the catalyst surface. The Rh^0 sites are particularly effective in dissociating H_2 into hydrogen atoms (H*, Fig. 12), which are crucial for the subsequent hydrogenation steps. Concurrently, CO_2 molecules interact with the surface, getting activated and possibly forming bent CO_2 species. This activation is essential for making CO_2 more reactive. In one route, the carbon dioxide can be dissociated on the rhodium sites, generating Rh-carbonyls in linear and bridged configuration (specie IA, Fig. 12). Another possible route involves the formation of formate intermediates (specie II, Fig. 12), especially facilitated by the ZrO_2 components (as detailed in Fig. 11a), which can be formed by the reduction (by H* atoms) of bicarbonate species (specie IB, Fig. 12), whose origin can be associated to the reaction between CO_{2gas} and Zr-OH groups. However, other proposals suggest that they can be produced by the migration of carbonyl species (species IA, Fig. 12) or CO_{gas} into the OH groups on the support (ZrO_2). Hence, two main intermediates are generated as result until this point. As discussed previously, we propose that the hydrogenation of formate species (species II, Fig. 12) can form methane. In contrast, COgas can be formed by carbonyls desorption on Rh sites (specie IA, Fig. 12). However, the production of CH_4 via hydrogenation of Rh-CO species cannot be ruled out completely.

4. Conclusions

This work investigated the effect of the incorporation of ZrO_2 on the surface of the Rh supported on SBA-15 catalysts via chemical grafting. The incorporation of zirconium oxide enhances the CO_2 conversion and promotes the catalysis of the CO_2 methanation instead of the RWGS reaction. FTIR studies reveal the formation of rhodium carbonyls in all samples, with the ZrO_2-containing samples also showing formate species formation. This suggests a ZrO_2-facilitated pathway for methane production, likely through the hydrogenation of formate intermediates. This study proposes that the presence of hydroxyl groups on ZrO_2 promotes their formation. This suggests that the methane formation could

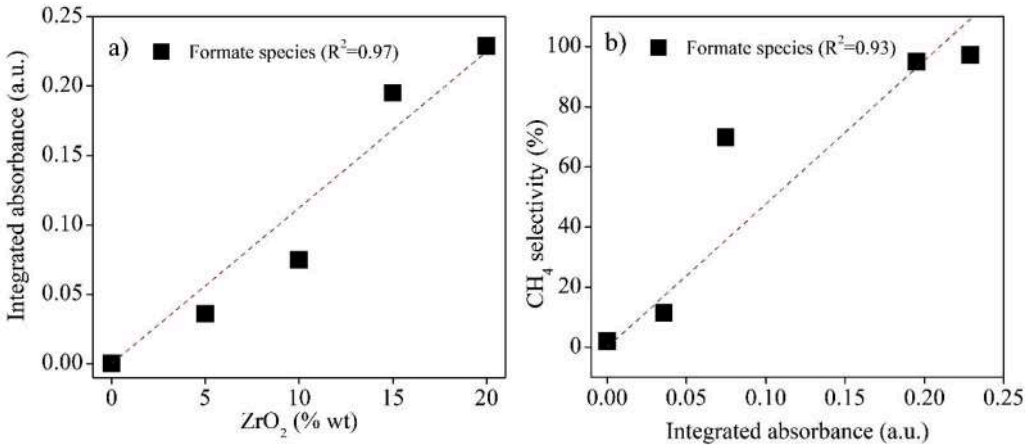

Fig. 11. Linear relations between a) ZrO_2 load and the maximum intensity of surface formate species; b) the maximum intensity of surface formate species and the selectivity towards CH_4 at 300°C.

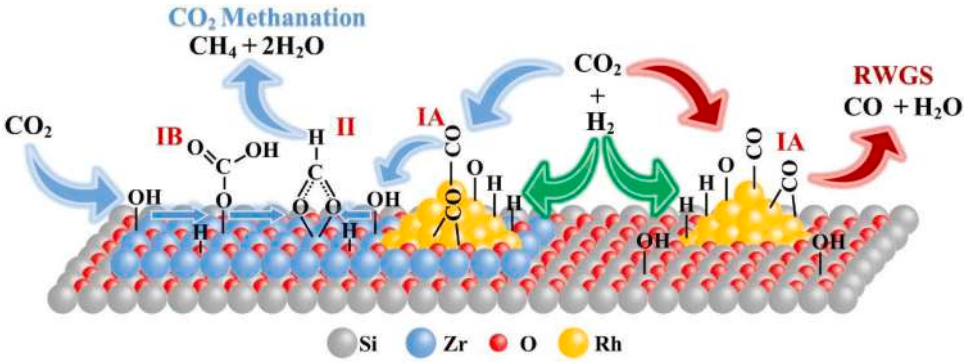

Fig. 12. Schematic representation of the CO_2 hydrogenation on Rh supported on ZrO_2-grafted SBA-15 catalysts.

be associated with the hydrogenation of formate species. The reaction pathway in the ZrO_2-free sample involves CO_2 undergoing dissociative adsorption on rhodium sites, forming carbonyl compounds and adsorbed oxygen ($O_{\_ads}$). These compounds are then released as carbon monoxide gas ($CO_{\_gas}$). In contrast, for the samples with grafted ZrO_2, the carbonyl species transition to Zr-OH groups, initiating the formation of formate species. These formate species interact with hydrogen (produced from the dissociation of H_2 on Rh) to yield methane. Additionally, the Zr-OH groups play an essential role in enhancing the formation of formate species through the interaction with bicarbonate species, demonstrating a distinct and more complex reaction pathway in the presence of ZrO_2.

CRediT authorship contribution statement

K.A. Gómez-Flores: Investigation. **A. Solís-García:** Writing – review & editing, Investigation. **S.A. Jimenez Lam:** Writing – review & editing, Methodology, Investigation. **M.E. Cervantes-Gaxiola:** Writing – review & editing, Methodology, Investigation. **R.I. Castillo-López:** Writing – review & editing, Methodology, Investigation. **J.P. Ruelas Leyva:** Writing – review & editing, Methodology, Investigation. **S.A. Gómez:** Writing – review & editing, Writing – original draft, Methodology, Investigation, Conceptualization. **E. Flores-Aquino:** Writing – review & editing, Methodology, Investigation. **T.A. Zepeda:** Writing – review & editing, Writing – original draft, Methodology, Investigation, Conceptualization.

Declaration of competing interest

The authors declare that they have no known competing financial interests or personal relationships that could have appeared to influence the work reported in this paper. Trino Zepeda reports financial support was provided by National Autonomous University of Mexico Center for Nanoscience and Nanotechnology.

Data availability

Data will be made available on request.

Acknowledgments

We thank DGAPA-UNAM project IN112922, IN101523 and IA100822. Thanks to project CONACYT-F003 117373 for their partial financial support. The authors thank Francisco Ruiz, David Dominguez, J. Mendoza, Israel Gradilla, Pedro Casillas, and Eloisa Aparicio for technical assistance.

References

[1] M. Abdallah, Y. Lin, R. Farrauto, Laboratory aging of a dual function material (DFM) washcoated monolith for varying ambient direct air capture of CO_2 and in situ catalytic conversion to CH_4, Appl. Catal. B. Environ. 339 (2023) 123105, https://doi.org/10.1016/j.apcatb.2023.123105.

[2] X. Wang, D. Hu, Y. Hao, L. Zhang, N. Sun, W. Wei, Continuous CO_2 abatement via integrated carbon capture and conversion over Ni-MgO-Al_2O_3 dual-functional materials, Sep. Purif. Technol. 322 (2023) 124295, https://doi.org/10.1016/j.seppur.2023.124295.

[3] Y. Xie, V. De Coster, L. Buelens, H. Poelman, B. Tunca, J.-W. Seo, C. Detavernier, V. Galvita, Tuning CO_2 methanation selectivity via MgO/Ni interfacial sites, J. Catal. 426 (2023) 162–172, https://doi.org/10.1016/j.jcat.2023.07.016.

[4] E. Harkou, S. Hafeez, P. Adamou, Z. Zhang, A.I. Tsiotsias, N.D. Charisiou, M. A. Goula, S.M. Al-Salem, G. Manos, A. Constantinou, Different reactor configurations for enhancement of CO_2 methanation, Environ. Res. 236 (2023) 116760, https://doi.org/10.1016/j.envres.2023.116760.

[5] Z. Refaat, M. El Saied, A.O. Abo El Naga, S.A. Shaban, H.B. Hassan, M. Refaat Shehata, F.Y. El Kady, Efficient CO_2 methanation using nickel nanoparticles supported mesoporous carbon nitride catalysts, Sci. Rep. 13 (2023) 4855, https://doi.org/10.1038/s41598-023-31958-1.

[6] L. Yang, S. Hong, Impact of the clean energy structure of building operation on the co-benefits of CO_2 and air pollutant emission reductions in Chinese provinces, J. Clean. Prod. 413 (2023) 137400, https://doi.org/10.1016/j.jclepro.2023.137400.

[7] K.K. Jaiswal, C.R. Chowdhury, D. Yadav, R. Verma, S. Dutta, K.S. Jaiswal, K.S. Kumar Karuppasamy SangmeshB, Renewable and sustainable clean energy development and impact on social, economic, and environmental health, Energy Nexus 7 (2022) 100118, https://doi.org/10.1016/j.nexus.2022.100118.

[8] S. Algarni, V. Tirth, T. Alqahtani, S. Alshehery, P. Kshirsagar, Contribution of renewable energy sources to the environmental impacts and economic benefits for sustainable development, Sustain. Energy Technol. Assess. 56 (2023) 103098, https://doi.org/10.1016/j.seta.2023.103098.

[9] L. Baharudin, N. Rahmat, N.H. Othman, N. Shah, S. Shatir, A. Syed-Hassan, Formation, control, and elimination of carbon on Ni-based catalyst during CO_2 and CH_4 conversion via dry reforming process: a review, J. CO_2 Util. 61 (2022) 102050, https://doi.org/10.1016/j.jcou.2022.102050.

[10] Y. Adekunle Alli, P. Olusakin Oladoye, O. Ejeromedoghene, O. Mutolib Bankole, O. Azeez Alimi, E. Oyinkansola Omotola, C. Ajibade Olanrewaju, K. Philippot, A. S. Adeleye, A. Sunday Ogunlaja, Nanomaterials as catalysts for CO_2 transformation into value-added products: A review, Sci. Total Environ. 868 (2023) 161547, https://doi.org/10.1016/j.scitotenv.2023.161547.

[11] A. Mustafa, B. Guene Lougou, Y. Shuai, Z. Wang, H. Tan, Current technology development for CO_2 utilization into solar fuels and chemicals: a review, J. Energy Chem. 49 (2020) 96–123, https://doi.org/10.1016/j.jechem.2020.01.023.

[12] L. Zhang, Z.-J. Zhao, J. Gong, Nanostrukturierte Materialien für die elektrokatalytische CO_2-Reduktion und ihre Reaktionsmechanismen, Angew. Chem. 129 (2017) 11482–11511, https://doi.org/10.1002/ange.201612214.

[13] P. Sabatier, J. Senderens, Comptes Rendus Des Séances De L'Académie Des Sciences, section VI–Chimie, Imprimerie Gauthier-Villars (1902). Paris.

[14] C. Choi, A. Khuenpetch, W. Zhang, S. Yasuda, Y. Li, H. Machida, H. Takano, K. Izumiya, Y. Kawajiri, K. Norinaga, Determination of kinetic parameters for CO_2 methanation (sabatier reaction) over Ni/ZrO_2 at a stoichiometric feed-gas composition under elevated pressure, Energy Fuels 35 (24) (2021) 20216–20223, https://doi.org/10.1021/acs.energyfuels.1c01534.

[15] P.J. Lunde, F.L. Kester, Rates of methane formation from carbon dioxide and hydrogen over a ruthenium catalyst, J. Catal. 30 (1973) 423–429, https://doi.org/10.1016/0021-9517(73)90159-0.

[16] V. Jiménez, P. Sánchez, P. Panagiotopoulou, J.L. Valverde, A. Romero, Methanation of CO, CO_2 and selective methanation of CO, in mixtures of CO and CO_2, over ruthenium carbon nanofibers catalysts, Appl. Catal. A Gen. 390 (2010) 35–44, https://doi.org/10.1016/j.apcata.2010.09.026.

[17] Y. Guo, S. Mei, K. Yuan, D.-J. Wang, H. Liu, C.-H. Yan, Y.-W. Zhang, Low-temperature CO_2 methanation over CeO_2-supported Ru single atoms, nanoclusters, and nanoparticles competitively tuned by strong metal–support interactions and H-

spillover effect, ACS Catal 8 (2018) 6203–6215, https://doi.org/10.1021/acscatal.7b04469.
[18] J. Xua, X. Su, H. Duan, B. Hou, Q. Lin, X. Liu, X. Pan, G. Pei, H. Geng, Y. Huang, T. Zhang, Influence of pretreatment temperature on catalytic performance of rutile TiO_2-supported ruthenium catalyst in CO_2 methanation, J. Catal. 333 (2016) 227–237, https://doi.org/10.1016/j.jcat.2015.10.025.
[19] A. Porta, L. Falbo, C.G. Visconti, L. Lietti, C. Bassano, P. Deiana, Synthesis of Ru-based catalysts for CO_2 methanation and experimental assessment of intraporous transport limitations, Catal. Today 343 (2020) 38–47, https://doi.org/10.1016/j.cattod.2019.01.042.
[20] F. Solymosi, A. Erdöhelyi, T. Bángági, Methanation of CO_2 on supported rhodium catalyst, J. Catal. 68 (1981) 371–382, https://doi.org/10.1016/0021-9517(81)90106-8.
[21] J.C. Matsubu, V.N. Yang, P. Christopher, Isolated metal active site concentration and stability control catalytic CO_2 reduction selectivity, J. Am. Chem. Soc. 137 (2015) 3076–3084, https://doi.org/10.1021/ja5128133.
[22] C. Wang, E. Guan, L. Wang, X. Chu, Z. Wu, J. Zhang, Z. Yang, Y. Jiang, L. Zhang, X. Meng, B.C. Gates, F.-S. Xiao, Product selectivity controlled by nanoporous environments in zeolite crystals enveloping rhodium nanoparticle catalysts for CO_2 hydrogenation, J. Am. Chem. Soc. 141 (2019) 8482–8488, https://doi.org/10.1021/jacs.9b01555.
[23] C. Schild, A. Wokaun, A. Baiker, Surface species in CO_2 methanation over amorphous palladium/zirconia catalysts, J. Molecul. Catal. 69 (1991) 347–357, https://doi.org/10.1016/0304-5102(91)80115-J.
[24] J.H. Kwak, L. Kovarik, J. Szanyi, Heterogeneous catalysis on atomically dispersed supported metals: CO_2 reduction on multifunctional Pd catalysts, ACS Catal 3 (2013) 2094–2100, https://doi.org/10.1021/cs4001392.
[25] X. Wang, H. Shi, J.H. Kwak, J. Szanyi, Rh-Catalysed direct cyclisation of 1,4-naphthoquinone and 9,10-phenanthraquinone with alkyne: facile access to 1,8-dioxapyrenes and 1,12-dioxaperylenes as orange and red-emitting luminophores, ACS Catal 5 (2015) 6337–6349, https://doi.org/10.1039/C5CC00312A.
[26] A. Solis-Garcia, J.F. Louvier-Hernandez, A. Almendarez-Camarillo, J.C. Fierro-Gonzalez, Participation of surface bicarbonate, formate and methoxy species in the carbon dioxide methanation catalyzed by ZrO_2-supported Ni, Appl. Catal. B Environ. 218 (2017) 611–620, https://doi.org/10.1016/j.apcatb.2017.06.063.
[27] Q. Pan, J. Peng, T. Sun, S. Wang, S. Wang, Insight into the reaction route of CO_2 methanation: promotion effect of medium basic sites, Catal. Commun. 45 (2014) 74–78, https://doi.org/10.1016/j.catcom.2013.10.034.
[28] L. Shen, J. Xu, M. Zhu, Y.-F. Han, Essential role of the support for nickel-based CO_2 methanation catalysts, ACS Catal 10 (2020) 14581–14591, https://doi.org/10.1021/acscatal.0c03471.
[29] P. Marocco, E.A. Morosanu, E. Giglio, D. Ferrero, C. Mebrahtu, A. Lanzini, S. Abate, S. Bensaid, S. Perathoner, M. Santarelli, R. Pirone, CO_2 methanation over Ni/Al hydrotalcite-derived catalyst: experimental characterization and kinetic study, Fuel 225 (2018) 230–242, https://doi.org/10.1016/j.fuel.2018.03.137.
[30] J. Li, Y. Lin, X. Pan, D. Miao, D. Ding, Y. Cui, J. Dong, X. Bao, Enhanced CO_2 methanation activity of Ni/anatase catalyst by tuning strong metal–support interactions, ACS Catal 9 (2019) 6342–6348, https://doi.org/10.1021/acscatal.9b00401.
[31] X. Jia, X. Zhang, N. Rui, X. Hu, C.-Jun Liu, Structural effect of Ni/ZrO_2 catalyst on CO_2 methanation with enhanced activity, Appl. Catal. B Environ. 244 (2019) 159–169, https://doi.org/10.1016/j.apcatb.2018.11.024.
[32] J. Tan, J. Wang, Z. Zhang, Z. Ma, L. Wang, Y. Liu, Highly dispersed and stable Ni nanoparticles confined by MgO on ZrO_2 for CO_2 methanation, Appl. Surf. Sci. 481 (2019) 1538–1548, https://doi.org/10.1016/j.apsusc.2019.03.217.
[33] F. Wang, S. He, H. Chen, B. Wang, L. Zheng, M. Wei, D.G. Evans, X. Duan, Active site dependent reaction mechanism over Ru/CeO_2 catalyst toward CO_2 methanation, J. Am. Chem. Soc. 138 (2016) 6298–6305, https://doi.org/10.1021/jacs.6b02762.
[34] Y. RP, Q. Li, T. Gong, T. Wang, J.J. Razink, L. Lin, Y.Y. Qin, Z. Zhou, H. Adidharma, J. Tang, A.G. Russell, M. Fan, Y.-G. Yao, High-performance of nanostructured Ni/CeO_2 catalyst on CO_2 methanation, Appl. Catal. B Environ. 268 (2020) 118474, https://doi.org/10.1016/j.apcatb.2019.118474.
[35] G. Zhou, H. Liu, K. Cui, A. Jia, G. Hu, Z. Jiao, Y. Liu, X. Zhang, Role of surface Ni and Ce species of Ni/CeO_2 catalyst in CO_2 methanation, Appl. Surf. Sci. 383 (2016) 248–252, https://doi.org/10.1016/j.apsusc.2016.04.180.
[36] M.C. Bacariza, I. Graça, J.M. Lopes, C. Henriques, Tuning zeolite properties towards CO_2 methanation: an overview, Chem. Cat. Chem. 11 (2019) 2388–2400, https://doi.org/10.1002/cctc.201900229.
[37] S. Scirè, C. Crisafulli, R. Maggiore, S. Minicò, S. Galvagno, Influence of the support on CO_2 methanation over Ru catalysts: an FT-IR study, Catal. Lett. 51 (1948) 41–45, https://doi.org/10.1023/A:1019028816154.
[38] M.-C. Silaghi, A. Comas-Vives, C. Copéret, CO_2 activation on Ni/γ–Al_2O_3 catalysts by first-principles calculations: From ideal surfaces to supported nanoparticles, ACS Catal 6 (2016) 4501–4505, https://doi.org/10.1021/acscatal.6b00822.
[39] C.-S. Chen, C.S. Budi, H.-C. Wu, D. Saikia, H.-M. Kao, Size-tunable Ni nanoparticles supported on surface-modified, cage-type mesoporous silica as highly active catalysts for CO_2 hydrogenation, ACS Catal 7 (2017) 8367–8381, https://doi.org/10.1021/acscatal.7b02310.
[40] F.Gao Zhen, B. Tian, P. Ding, Y. Deng, Z. Li, H. Gao, G. Lu, Enhancing activity for carbon dioxide methanation by encapsulating (1 1 1) facet Ni particle in metal–organic frameworks at low temperature, J. Catal. 348 (2017) 200–211, https://doi.org/10.1016/j.jcat.2017.02.031.
[41] W. Zhen, B. Li, G. Lu, J. Ma, Enhancing catalytic activity and stability for CO_2 methanation on Ni@MOF-5 via control of active species dispersion, Chem. Commun. 51 (2015) 1728–1731, https://doi.org/10.1039/C4CC08733J.
[42] L. Shen, J. Xu, M. Zhu, Y.-F. Han, Essential role of the support for nickel-based CO_2 methanation catalysts, ACS Catal. 10 (2020) 14581–14591, https://doi.org/10.1021/acscatal.0c03471.
[43] S. Kattel, P. Liu, J.G. Chen, Tuning selectivity of CO2 hydrogenation reactions at the metal/oxide interface, J. Am. Chem. Soc. 139 (2017) 9739–9754, https://doi.org/10.1021/jacs.7b05362.
[44] A. Solis-Garcia, T.A. Zepeda, J.C. Fierro-Gonzalez, Spectroscopic evidence of surface species during CO_2 methanation catalyzed by supported metals: A review, Catal. Today 394-396 (2022) 2–12, https://doi.org/10.1016/j.cattod.2021.10.015.
[45] A. Solis-Garcia, T.A. Zepeda, J.C. Fierro-Gonzalez, Spectroscopic evidence of the simultaneous participation of rhodium carbonyls and surface formate species during the CO_2 methanation catalyzed by ZrO_2-supported Rh, Appl. Catal. B. Environ. 304 (2022) 120955, https://doi.org/10.1016/j.apcatb.2021.120955.
[46] E.M. Mendoza-Núñez, J.C. Fierro-Gonzalez, T.A. Zepeda, A. Solis-Garcia, Effect of platinum addition on the reaction mechanism of the CO_2 methanation catalyzed by ZrO_2-supported Rh, Mol. Catal. 533 (2022) 112801, https://doi.org/10.1016/j.mcat.2022.112801.
[47] M. Jia, P. Afanasiev, M. Vrinat, The influence of preparation method on the properties of NiMo sulfide catalysts supported on ZrO2, Appl. Catal. A. Gen. 278 (2005) 213–221, https://doi.org/10.1016/j.apcata.2004.09.037.
[48] J.-H. Lee, C.-H. Shin, Y.-W. Suh, Higher Brønsted acidity of WOx/ZrO2 catalysts prepared using a high-surface-area zirconium oxyhydroxide, Mol. Catal. 438 (2017) 272–279, https://doi.org/10.1016/j.mcat.2017.06.012.
[49] R. Tang, N. Ullah, Z. Li, Unveiling the promotion effect of Zr species on SBA-15 supported nickel catalysts for CO_2 methanation, Int. J. Hydrog. 48 (2023) 4694–4707, https://doi.org/10.1016/j.ijhydene.2022.11.011.
[50] M.E.Gálvez Albarazi, P. Da Costa, Synthesis strategies of ceria–zirconia doped Ni/SBA-15 catalysts for methane dry reforming, Catal. Comm. 59 (2015) 108–112, https://doi.org/10.1016/j.catcom.2014.09.050.
[51] J. Colmenares-Zerpa, J. Gajardo, A.F. Peixoto, D.S.A. Silva, J.A. Silva, F. Gispert-Guirado, J. Llorca, E.A. Urquieta-Gonzalez, J.B.O. Santos, R.J. Chimentão, High zirconium loads in Zr-SBA-15 mesoporous materials prepared by direct-synthesis and pH-adjusting approaches, J. Solid State Chem. 312 (2022) 123296, https://doi.org/10.1016/j.jssc.2022.123296.
[52] O.Y. Gutierrez, G.A. Fuentes, C. Salcedo, T. Klimova, SBA-15 supports modified by Ti and Zr grafting for NiMo hydrodesulfurization catalysts, Catal. Today 116 (2006) 485–497, https://doi.org/10.1016/S1387-1811(01)00202-5.
[53] J.A. Colín-Luna, G.E. Zamora-Rodea, A.K. Medina-Mendoza, L. Alvarado-Perea, C. Angeles-Chávez, J. Escobar, J.G. Pacheco-Sosa, J.C. García Martínez, Zn supported on Zr modified mesoporous SBA-15 as sorbents of pollutant precursors contained in fossil fuels: Si/Zr ratio effect, Catal. Today 353 (2020) 63–72, https://doi.org/10.1016/j.cattod.2019.10.023.
[54] M. Olejniczak, M. Ziolek, Comparative study of Zr, Nb, Mo containing SBA-15 grafted with amino-organosilanes, Micropor. Mesopor. Mat. 196 (2014) 243–253, https://doi.org/10.1016/j.micromeso.2014.05.018.
[55] Y. Zhu, L. Jin, Y. Wang, B. Hu, J. Li, B. Hu, X. Liu, Selective catalytic oxidation of phenylcarbinol with Fe-doped Cu/SBA-15 catalyst: a study on the synergistic effect of Cu-Fe metals, Molecular Catalysis 551 (2023) 113649, https://doi.org/10.1016/j.mcat.2023.113649.
[56] S. Miao, Y. Wang, Y. Zhang, F. Lian, M. Li, Instantaneous and efficient removal of glyphosate with low concentration by amine-functionalized SBA-15 chelated with Fe(III), J. Environ. Chem. Eng. 11 (2023) 111004, https://doi.org/10.1016/j.jece.2023.111004.
[57] M.-M. Yang, H.-L. Su, D.-H. Yang, Z.-Y. Chen, L.-P. Wang, G. Li, Separable and recyclable SBA-15 based catalyst for metal-free ATRP, Eur. Polym. J. 196 (2023) 112299, https://doi.org/10.1016/j.eurpolymj.2023.112299.
[58] J. Colmenares-Zerpa, J. Gajardo, A.F. Peixoto, D.S.A. Silva, J.A. Silva, F. Gispert-Guirado, J. Llorca, E.A. Urquieta-Gonzalez, J.B.O. Santos, R.J. Chimentão, High zirconium loads in Zr-SBA-15 mesoporous materials prepared by direct-synthesis and pH-adjusting approaches, J. Solid State Chem. 312 (2022) 123296, https://doi.org/10.1016/j.jssc.2022.123296.
[59] B.L. Newalkar, S. Komarneni, Control over Microporosity of ORDERED Microporous−Mesoporous silica SBA-15 framework under microwave-hydrothermal conditions: effect of salt addition, Chem. Mater. 13 (2001) 4573–4579, https://doi.org/10.1021/cm0103038.
[60] A. Sabbaghi, F.L.Y. Lam, X. Hu, Zr-SBA-15 supported Ni catalysts for lean NOx reduction, J. Mol. Catal. A Chem. 409 (2015) 69–78, https://doi.org/10.1016/j.molcata.2015.08.005.
[61] D. Ding, J. Yu, Q. Guo, X. Guo, H. Mao, D. Mao, Highly efficient synthesis of C^{2+} oxygenates from CO Hydrogenation Over Rh–Mn–Li/SiO_2 catalyst: the effect of TiO_2 Promoter, Catal. Lett. 148 (2018) 2619–2626, https://doi.org/10.1007/s10562-018-2444-y.
[62] E. Sheerin, G.K. Reddy, P. Smirniotis, Evaluation of Rh/$Ce_xTi1-xO_2$ catalysts for synthesis of oxygenates from syngas using XPS and TPR techniques, Catal. Today 263 (2016) 75–83, https://doi.org/10.1016/j.cattod.2015.07.050.
[63] M. Jin, Y. Song, C. Wang, Z. Shen, Y. Zhang, Catalytic transfer hydrogenation of CO_2 to formic acid with glycerol as the hydrogen donor over Ru-REUSY catalysts, Molecular Catalysis 551 (2023) 113655, https://doi.org/10.1016/j.mcat.2023.113655.
[64] Y. Gangarajula, F. Hong, Q. Li, X. Jiang, W. Liu, M. Akri, Y. Su, Y. Zhang, L. Li, B. Qiao, Operando Induced Strong Metal-Support Interaction of Rh/CeO_2 Catalyst in Dry Reforming of Methane, Appl. Catal. B Environ. (2023) 123503, https://doi.org/10.1016/j.apcatb.2023.123503.
[65] K.-R. Hwang, S.-K. Ihm, S.-C. Park, J.-S. Park, Pt/ZrO_2 catalyst for a single-stage water-gas shift reaction: Ti addition effect, Int. J. Hydrogen Energy. 38 (2013) 6044–6051, https://doi.org/10.1016/j.ijhydene.2013.01.101.

[66] P. Santos Querino, J.R.C. Bispo, M. do Carmo Rangel, The effect of cerium on the properties of Pt/ZrO2 catalysts in the WGSR, Catal. Today 107-108 (2005) 920–925, https://doi.org/10.1016/j.cattod.2005.07.032.
[67] S.N Bukhari, C.C. Chong, H.D. Setiabudi, Y.W. Cheng, L. P.Teh, A.A A.A.Jalil, Ni/Fibrous type SBA-15: highly active and coke resistant catalyst for CO2 methanation, Chem. Eng. Sci. 229 (2021) 116141, https://doi.org/10.1016/j.ces.2020.116141.
[68] R.F. Van Slooten, B.E. Nieuwenhuys, An infrared study of the interaction of CO and NO with a silica supported Pt-Rh alloy catalyst, J. Catal. 122 (1990) 429–437, https://doi.org/10.1016/0021-9517(90)90296-V.
[69] L.F. Bobadilla, V. Garcilaso, M.A. Centeno, J.A. Odriozola, Monitoring the reaction mechanism in model biogas reforming by in situ transient and steady-state DRIFTS measurements, ChemSusChem 10 (2017) 1193–1201, https://doi.org/10.1002/cssc.201601379.
[70] R. Tang, N. Ullah, Z. Li, Unveiling the promotion effect of Zr species on SBA-15 supported nickel catalysts for CO2 methanation, Int. J. Hydrogen Energy 48 (2023) 4694–4707, https://doi.org/10.1016/j.ijhydene.2022.11.011.
[71] P. Campani, C.S. Fang, H.W. Prengle, Infrared absorption coefficients for certain pollutant gases, Appl. Spectrosc. 26 (1972) 372–378, https://doi.org/10.1366/000370272774352119.
[72] I.A. Fisher, A.T. Bell, A mechanistic study of methanol decomposition over Cu/SiO2, ZrO2/SiO2, and Cu/ZrO2/SiO2, J. Catal. 184 (1999) 357–376, https://doi.org/10.1006/jcat.1999.2420.
[73] G. Busca, J. Lamotte, J.C. Lavalley, V. Lorenzelli, V. FT-IR study of the adsorption and transformation of formaldehyde on oxide surfaces, J. Am. Chem. Soc. 109 (1987) 5197–5202, https://doi.org/10.1021/ja00251a025.
[74] E.M. Mendoza-Núñez, J.C. Fierro-Gonzalez, T.A. Zepeda, A. Solis-Garcia, Effect of platinum addition on the reaction mechanism of the CO2 methanation catalyzed by ZrO2-supported Rh, Mol. Catal. 533 (2022) 112801, https://doi.org/10.1016/j.mcat.2022.112801.
[75] X. Wang, H. Shi, J.H. Kwak, J. Szanyi, Mechanism of CO2 hydrogenation on Pd/Al2O3 catalysts: kinetics and transient DRIFTS-MS studies, Acs Catal. 5 (2015) 6337–6349, https://doi.org/10.1021/acscatal.5b01464.
[76] M. Daturi, C. Binet, J.C. Lavalley, G. Blanchard, Surface FTIR investigations on CexZr1− xO2 system, Surf. Interface Anal.: Int. J. Devot. Dev. Appl. Tech. Anal. Surf., Interf., Films 30 (2000) 273–277, https://doi.org/10.1002/1096-9918(200008)30. :1%3C273::AID-SIA715%3E3.0.CO;2-G.
[77] J. Gajardo, J. Colmenares-Zerpa, A.F. Peixoto, D.S.A. Silva, J.A. Silva, F. Gispert-Guirado, E.A. Urquieta-Gonzalez, J.B.O. Santos, J. Szanyi, C. Sepúlveda, M. G. Álvarez, R.J. Chimentão, J R, Revealing the effects of high Al loading incorporation in the SBA-15 silica mesoporous material, J. Porous Mater. 30 (2023) 1–21, https://doi.org/10.1007/s10934-023-01453-z (2023)1687–1707 *Journal of Porous Materials*.
[78] K. Föttinger, W. Emhofer, D. Lennon, G Rupprechter, Adsorption and Reaction of CO on (Pd–) Al 2 O 3 and (Pd–) ZrO 2: Vibrational Spectroscopy of Carbonate Formation, Topic. Catal. 60 (2017) 1722–1734, https://doi.org/10.1007/s11244-017-0852-7, 2017.